Journal of Marine Science and Application (2026) 25: 423-432
https://doi.org/10.1007/s11804-025-00709-1

RESEARCH ARTICLE

Supercavity Enhancement in High-Speed Heavyweight Torpedoes: Exploring the Role of Secondary Cavitator

Kumar Gaurav[1], **Nagothu Venkatesh**[1], **Aman Raj**[1] and **Ashish Karn**[1]

Received: 06 February 2025 / Accepted: 07 May 2025

Abstract

Underwater warfare in the modern world demands the development of fast, supercavitating torpedoes. Torpedoes typically achieve supercavitation via a single cavitator mounted at the nose; the cavitator's dimensions dictate the supercavity size. This study introduces a novel approach of incorporating a secondary cavitator to enhance the supercavity and improve the performance of supercavitating torpedoes. Numerical simulations are performed using Reynolds-averaged Navier – Stokes equations solved with a pressure-based algorithm. The volume of fluid (VOF) multiphase model, in conjunction with the Schnerr–Sauer cavitation model, is employed to model the supercavitation phenomenon. The effects of cavitator size, positioning, and operating conditions on supercavity behavior are also examined. Results indicate that positioning the secondary cavitator at 70%–90% of the primary supercavity length significantly enlarges the supercavity, achieving a 30%–35% increase in supercavity length. The optimal size for the secondary cavitator is also identified, beyond which reverse flow and cavity shrinkage occur. The dependence of the secondary cavitator's critical size on the primary cavitator's diameter and Froude number is further investigated. This research provides new insights into the design of supercavitating vehicles and establishes a framework for optimizing cavitator configurations in heavyweight torpedoes.

Keywords Supercavitation; High-speed torpedo; Multiphase flow; Cavitator; Cavity enlargement; Underwater vehicles

1 Introduction

Supercavitation is a remarkable hydrodynamic phenomenon with significant advantages for high-speed underwater travel. An object, such as a torpedo or submarine, is enveloped within a vapor-filled cavity. This cavity minimizes the contact area between the object and the surrounding liquid, drastically reducing the drag forces and allowing for higher speeds than those achievable with conventional hydrodynamic designs (Karn and Chawdhary, 2018; Nesteruk, 2012). A supercavity forms when the pressure around the object drops below the liquid's vapor pressure, causing vaporization and creating numerous small cavitation bubbles (Cao et al., 2017). These bubbles coalesce into a large vapor cavity, producing the supercavitation effect (Karn and Rosiejka, 2017; Logvinovich and Serebryakov, 1975).

Supercavitation has vast potential applications, particularly in naval defense and transport sectors, where drag reduction for submerged vehicles offers substantial performance enhancements. In the defense sector, supercavitating torpedoes and submarines can travel at higher speeds than conventional vehicles, providing efficiency and tactical advantages (Alyanak et al., 2006). Supercavitation also plays a vital role in naval transportation applications, such as in the design of hydrofoils, where it improves vessel efficiency by reducing water resistance (Xu and Khoo, 2020). Beyond transportation, supercavitation has also been explored in other fields, such as aeration, desalination, and wastewater treatment, where the cavitation effect enhances contaminant removal and increases process efficiency (Dular et al., 2016; Likhachev et al., 2014; Schmid, 2010). A parametric study on the effect of cavitation gener-

Article Highlights

- This study introduces a novel approach to enhance supercavity in supercavitating torpedoes using a secondary cavitator.
- It demonstrates that secondary cavitators positioned at 70%–90% of the primary supercavity length provide the highest enlargement to the supercavity.
- We identifies the critical size of the secondary cavitator: below this threshold, it merges with the primary supercavity; above it, it suppresses the primary cavity.
- This study analyses the influence of primary cavitator size and Froude number on supercavity characteristics.
- This study contributes to the design of more efficient torpedoes for high-speed naval applications.

✉ Ashish Karn
akarn@ddn.upes.ac.in

[1] Department of Aerospace Engineering, Mechanical Cluster, School of Advanced Engineering, UPES, Dehradun, Uttarakhand 248007, India

ation unit (CGU) design on hydrodynamic cavitation efficiency found that a hemispherical-shaped CGU exhibited the highest cavitation efficiency (Sun et al., 2021).

Supercavity enlargement has been a focal research point in underwater propulsion systems, with the primary goal of improving efficiency and performance. Inviscid models have been developed to predict supercavity geometries across a wide range of Froude numbers, producing accurate predictions of supercavity morphologies (Yi et al., 2022). Given that supercavities are formed by the coalescence of numerous small bubbles, the empirical models originally developed for estimating elongated bubbles from gas injection (Gaurav et al., 2022) have been extended to artificial supercavity sizes.

Extensive research has been conducted to optimize cavitator shapes for supercavity enlargement, with investigations covering various geometries including disk, spherical, conical, and elliptical cavitators (Chen et al., 2023; Gaurav et al., 2024; Kim et al., 2021; Shao et al., 2020). The effects of varying cone angles on supercavitation characteristics have been further explored (Jeong et al., 2024). A conical head-shaped projectile has been found to demonstrate good hydrodynamic performance during high-speed entry (Park et al., 2024). In efforts to artificially extend the supercavity, researchers have explored revolving nonaxisymmetric cavitators and developed an elliptical cavitator for nonaxisymmetric underwater vehicles with a detachable fairing to reduce wetted-state drag while ensuring a smooth transition to supercavitation (Chen et al., 2023). Although this instrument slightly increases drag, it significantly elongates the supercavity compared with that formed by conventional disc cavitators under the same drag conditions (Kim et al., 2022). Other mechanisms, such as the use of hot working fluid, microbubbles, and textured surfaces, have also been employed to increase supercavity size (Liu et al., 2023; Rajkumar et al., 2023). Researchers have also utilized cavitators to design antiroll fins that improve the maneuverability and roll control of the vehicle. An antiroll fin significantly enhances rudder efficiency and reduces the destabilizing moment, enabling a finless supercavitating vehicle (SV) design (Li et al., 2022). Supercavitation under supersonic conditions has also been investigated using numerical methods. The results show that high speeds cause an extreme temperature rise at the stagnation point, indicating the necessity of effective cooling techniques to avoid projectile damage and metal softening (Nguyen ang Park, 2022). This body of work underscores the critical importance of supercavity enhancement in a wide range of applications.

A key limitation of single cavitators is that they often fail to generate sufficiently large supercavities, particularly at low operational speeds. In such cases, portions of the vehicle's surface remain exposed to the fluid, resulting in undesirably high drag. Moreover, high speeds are difficult to achieve due to propulsion limitations and material strength. These challenges highlight the need for new strategies that can enhance supercavity size and stability.

One promising solution is the use of a secondary cavitator, positioned downstream of the primary cavitator, to further increase the supercavity size. Secondary cavitators interact with the primary supercavity, extending its length and thereby reducing drag on the vehicle. This concept introduces new design possibilities for supercavitating vehicles; however, the optimal placement and sizing of the secondary cavitator remain unclear. Factors such as flow velocity and depth also influence the effectiveness of the secondary cavitator. Therefore, understanding the interactions between primary and secondary cavitators under different flow conditions is crucial for developing effective designs. A deep investigation into these interactions can lead to the development of robust designs for supercavitating vehicles, particularly in naval applications where maintaining high speeds is critical.

In this study, a detailed numerical investigation into the effects of secondary cavitators on supercavity size in heavyweight torpedoes is conducted. A 2D axisymmetric Reynolds-averaged Navier−Stokes (RANS) model is used to investigate the performance of various cavitator configurations, focusing on the size, positioning, and operating conditions required to optimize supercavity formation. By analyzing the influence of key parameters, this study aims to identify the optimal cavitator configuration to maximize the supercavity size. The findings provide insights for improving the performance of supercavitating vehicles and offer a practical framework for designing efficient underwater propulsion systems.

2 Methodology

Simulations are performed using ANSYS Fluent by solving the axisymmetric RANS equations coupled with the realizable k–ε turbulence model. The VOF multiphase model, combined with the Schnerr−Sauer cavitation model, is employed to capture the complex interactions between the vapor and liquid phases during supercavity formation. A grid independence test and a validation of the computational model against available experimental data are conducted to ensure the accuracy and reliability of the results.

For torpedoes with a primary cavitator, the supercavity size depends on the size of the primary cavitator (d_{pc}) and vehicle (d_v) and the velocity (U), fluid properties, and depth (h) of the torpedo. These parameters can be consolidated into two nondimensional parameters, i.e., Froude number defined as $Fr = U/\sqrt{\mathrm{gh}}$ and ratio of the primary cavitator's to the vehicle's diameter ($\tilde{d}_{\mathrm{cv}} = d_{\mathrm{pc}}/d_v$). If a secondary cavitator is introduced, then the supercavity size will depend on the secondary cavitator's height (h_{sc}), which can be converted to a nondimensional form using the primary cavitator's diameter ($\tilde{d}_{\mathrm{sp}} = h_{\mathrm{sc}}/d_{\mathrm{pc}}$). In this investigation, simulations are conducted on multiple cavitator sizes at Froude numbers ranging from 5 to 6. The Froude number is varied by changing the velocity of the freestream flow. $\tilde{d}_{\mathrm{cv}}$ ranges from 0.4 to 0.5, and $\tilde{d}_{\mathrm{sp}}$ ranges from 0 to 0.8. The Reynolds number of the flow is determined based on the primary cavitator's diameter as $Re = \rho V d_{\mathrm{pc}}/\mu$, where μ is the dynamic viscosity of the freestream flow. In this study, simulations are conducted at Reynolds numbers ranging from 1.78×10^7 to 2.67×10^7.

2.1 Geometry

The torpedo geometry is chosen on the basis of survey results for various heavyweight torpedoes from different nations. The final torpedo design measures 8 m in length and 800 mm in diameter. The torpedo's nose and tail shape is designed using Eqs. (1) and (2), respectively, to minimize drag on the body (Myring, 1976):

$$y_n = \frac{1}{2} d \left[1 - \left(\frac{x-a}{a}\right)^2\right]^{1/n} \tag{1}$$

$$y_t = \frac{1}{2} d - \left(\frac{3d}{2c^2} - \frac{\tan\theta}{c}\right)(x-a-b)^2 + \left(\frac{d}{c^3} - \frac{\tan\theta}{c^2}\right)(x-a-b)^3 \tag{2}$$

where y_n and y_t are the y locations of the nose and tail curves, respectively; a, b, and c are the lengths of nose, main body, and tail of the torpedo, respectively; d is the maximum diameter of the torpedo; and θ is the half-angle made by the tail as illustrated in Figure 1. The bluntness of the nose is governed by the variable n, whose large values indicate a highly blunted nose.

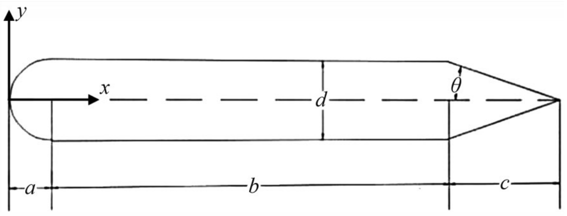

Figure 1 Torpedo geometrical parameters

A 150 mm-long circular rod connects the torpedo's nose to the cavitator body. A disc-shaped cavitator is used to produce a supercavity around the torpedo. The diameters of the torpedo and primary cavitator are denoted by d_v and d_{pc}, respectively. The height of the secondary cavitator is represented by h_{sc} as illustrated in Figure 2.

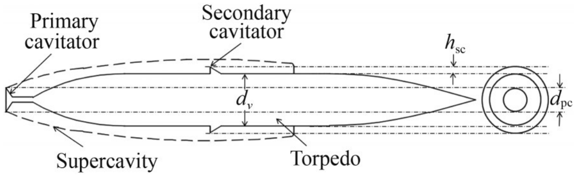

Figure 2 Torpedo installed with primary and secondary cavitators

The ratio of the primary cavitator's diameter to the torpedo diameter is defined as $\tilde{d}_{\mathrm{cv}}$. The experiment is conducted on the primary cavitator with three different diameters $\tilde{d}_{\mathrm{cv}}$ of 0.40, 0.45, and 0.50. The secondary cavitator is positioned at 35%, 45%, 55%, and 65% of the torpedo's length. The ratio of the secondary cavitator's height to the primary cavitator's diameter is defined as $\tilde{d}_{\mathrm{sp}}$. The study is carried out on eight different secondary cavitator sizes within the range of $\tilde{d}_{\mathrm{sp}} = 0.01\text{–}0.08$.

2.2 Meshing

A grid independence study is performed to finalize the mesh. Three structured meshes with different numbers of elements are utilized. The coarse mesh consists of approximately 43000 elements, and the medium mesh has an increased element count by a factor of 1.42, resulting in 61000 elements. The fine mesh comprises 87000 elements. Table 1 presents the detailed characteristics of the meshes used in the grid independence test.

Table 1 Properties of meshes used for grid independence test

Mesh	No. of elements	Wall distance (m)	Y^+ Value
Coarse mesh	43000	6.7×10^{-5}	150
Medium mesh	61000	4.5×10^{-5}	100
Fine mesh	87000	1.8×10^{-5}	40

The simulation is conducted at Froude numbers (Fr) ranging from 5 to 6 on a torpedo that only has a primary cavitator with a diameter ($\tilde{d}_{\mathrm{cv}}$) of 0.5. Cavitation is considered to occur in regions where the vapor volume fraction exceeds 50%. The supercavity shape is determined by isolating the regions where the vapor volume fraction is greater than 0.5.

In this study, the maximum horizontal length of the supercavity is considered the cavitation length. The nondimensional supercavity length is estimated as $\tilde{L} = L/d_{\mathrm{pc}}$, where L is the supercavity length, and d_{pc} is the primary cavitator's diameter. The values of $\tilde{L}$ obtained for different meshes and Froude numbers are plotted in Figure 3. The nondimensional supercavity length for the coarse mesh is shorter than those for the medium and fine meshes but is nearly identical between the medium and fine meshes.

On the basis of the grid independence test results, the medium mesh consisting of approximately 61000 elements

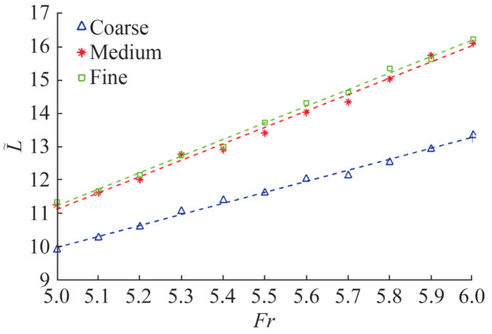

Figure 3 Variation of nondimensional supercavity length $\left(\tilde{L}\right)$ with Froude number for various meshes

is selected for further analysis. As shown in Figure 4(a), the final mesh is fine near the solid surface to capture the boundary layer. The element size grows at a rate of 1.2 as shown in Figure 4(b). The first cell height is chosen based on the Reynolds number range. The smallest element placed on the solid surface corresponds to a y^+ value of 100, which lies outside the viscous sublayer. The flow properties within the viscous sublayer are computed using the wall function. The computational domain is extended from $-L$ to $6L$, where L is the length of the torpedo.

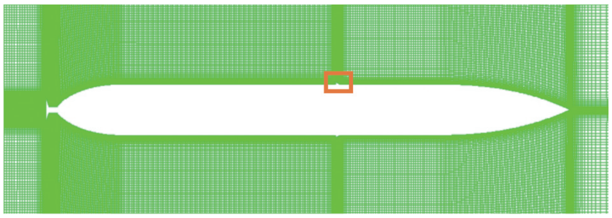

(a) Meshing of torpedo and primary cavitator

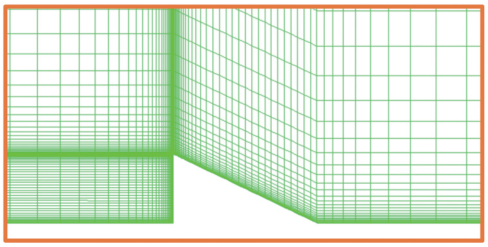

(b) Closeup view of the mesh near the secondary cavitator

Figure 4 Spatial discretization of the computational domain

2.3 Computational setup

Computations are carried out on ANSYS Fluent software. The 2D steady axisymmetric computational model is used for the simulations. Computations are based on the solution of RANS equations (Eqs. (3)–(4)) obtained using a pressure-based algorithm.

$$\frac{\partial \bar{\rho}}{\partial t} + \nabla .\left(\bar{\rho}\,\bar{U}\right) = 0 \tag{3}$$

$$\frac{\partial\left(\bar{\rho}\,\overline{U_i}\right)}{\partial t} + \nabla .\left(\bar{\rho}\,\overline{U_i}\,\bar{U}\right) = -\frac{\partial \bar{P}}{\partial x_i} + \frac{\partial}{\partial x_j}\left[\mu\left(\frac{\partial \overline{U_i}}{\partial x_j} + \frac{\partial \overline{U_j}}{\partial x_i}\right) - \overline{\rho u_i' u_j'}\right] \tag{4}$$

where $\bar{\rho}$, $\bar{U}$, and $\bar{P}$ are the mean density, velocity, and pressure of the flow, respectively; and $\rho u_i' u_j'$ represents the Reynolds stress tensor. A coupled scheme is utilized for the coupling of velocity and pressure terms. Gradients are evaluated using the least squares cell-based method.

In this investigation, seawater and water vapor are the primary and secondary phase materials, respectively. Their properties are defined in Table 2. The simulations are conducted at an operating pressure of 201 681 Pa, which corresponds to the pressure at a depth of 10 m and operating temperature of 298 K, and at flow velocities ranging from 47.5 to 60 m/s. The boundary conditions for the inlet and outlet are velocity inlet and pressure outlet, respectively. The numerical method employs a coupled least-order cell-based pressure–velocity solution using the PRESTO scheme. The volume fraction is modeled with a compressive scheme, and momentum is discretized using the second-order upwind method. The turbulent dissipation rate and turbulent kinetic energy ($k-\varepsilon$) are calculated using first-order upwind, and the energy equation is solved with second-order upwind.

Table 2 Properties of seawater used in computations

Fluid Property	Value
Density $\left(\rho, \text{kg/m}^3\right)$	1 023
Dynamic viscosity (u, kg/(ms))	9.2×10^{-4}
Saturation pressure (Pa)	3 494
Specific heat (c_p J/(kg·K))	4 010

The VOF equations are solved using the implicit volume fraction formulation to account for multiphase flow dynamics. The transport equations for the volume fraction of the liquid and vapor phases are expressed in Eqs. (5) and (6), respectively.

$$\frac{1}{\rho_v}\left[\frac{\partial\left(\alpha_v \rho_v\right)}{\partial t} + \frac{\partial}{\partial x_i}\left(\alpha_v \rho_v U\right)\right] = \frac{\dot{m}}{\rho_v} \tag{5}$$

$$\alpha_l = 1 - \alpha_v \tag{6}$$

where α_l and α_v denote the volume fraction of the liquid and vapor phases, respectively; ρ_l and ρ_v represent the density of liquid and vapor phases, respectively; $\dot{m}$ denotes the mass transfer rate per unit volume caused by cavitation between the liquid and vapor phases.

Cavitation is responsible for the mass transfer between the liquid and vapor phases. The mass transfer rate between the cavitation phases is estimated using the Schnerr–Sauer cavitation model (Schnerr and Sauer, 2001). In this cavitation model, a correlation between bubble growth and volume fraction change rate is established using Eqs. (7) and (8):

For $p > p_v$

$$\dot{m}^{+} = C_c \frac{\rho_v \rho_l}{\rho} \alpha_v \left(1 - \alpha_v\right) \frac{3}{R} \sqrt{\frac{2}{3} \frac{p - p_v}{\rho_l}} \tag{7}$$

For $p < p_v$

$$\dot{m}^{-} = C_v \frac{\rho_v \rho_l}{\rho} \alpha_v \left(1 - \alpha_v\right) \frac{3}{R} \sqrt{\frac{2}{3} \frac{p - p_v}{\rho_l}} \tag{8}$$

where R stands for the bubble radius, p is the static pressure, p_v is the vapor pressure, ρ_l is the density of the liquid, α_v is the vapor volume fraction, and C_c and C_v are the coefficients for the cavitation model. The bubble radius (R) in the above equation can be estimated through bubble number density (n) using Eq. (9):

$$R = \left[\frac{\alpha_v}{1 - \alpha_v} \frac{3}{4\pi n} \right]^{1/3} \tag{9}$$

For this investigation, n is considered as 10^{11}, and C_c and C_v are taken as 1.

Given that cavitation is generally considered a high-turbulence phenomenon, turbulence modeling is important and must be accurately addressed in addition to the cavitation model. In this study, the realizable k–ε model is employed to predict the turbulence effect outside the viscous sublayer. The wall function is used to model the turbulence properties inside the viscous sublayer. The transport equations for the realizable k–ε model are provided in Eqs. (10) and (11):

$$\frac{\partial(\rho k)}{\partial t} + \frac{\partial}{\partial x_j}\left(\rho k U_j\right) = \frac{\partial}{\partial x_j}\left[\left(\mu + \frac{\mu_t}{\sigma_k}\right)\frac{\partial k}{\partial x_j}\right] - \rho\varepsilon + \rho\beta^{*} k\varepsilon \tag{10}$$

$$\frac{\partial(\rho \varepsilon)}{\partial t} + \frac{\partial}{\partial x_j}\left(\rho \varepsilon U_j\right) = \frac{\partial}{\partial x_j}\left[\left(\mu + \frac{\mu_t}{\sigma_\varepsilon}\right)\frac{\partial \varepsilon}{\partial x_j}\right] - \rho\varepsilon C_{\varepsilon 1} P + \rho C_{\varepsilon 2} \frac{\varepsilon^2}{k} \tag{11}$$

where μ_t is the turbulent viscosity; σ_k and σ_ε are Prandtl numbers for k and ε, respectively; β^{*}, $C_{\varepsilon 1}$, and $C_{\varepsilon 2}$ are model constants; P represents the production of turbulent kinetic energy due to mean velocity gradients.

2.4 Validation of numerical model

The accuracy and reliability of the numerical model in this study are rigorously validated against the experiments conducted by Waid (1957). In the reference article, the authors investigated supercavitation characteristics for disc cavitators with diameters of 12.7, 19.05, and 25.4 mm. The freestream velocity varied between 3.66 and 7.32 m/s, corresponding to cavitation numbers ranging from 0.035 to 0.172. In the present study, computational results are compared for the cavitator diameter of 25.4 mm across various cavitation numbers. For the present validation, the cavitation number is calculated as $\sigma_c = \left(p - p_v\right)/0.5\rho V^2$, where p_v is the vapor pressure of the liquid; and p, ρ, and V are the static pressure, density, and velocity of the freestream flow, respectively. The half-length and maximum diameter of the supercavity are converted to nondimensional form by dividing them by the primary cavitator's diameter. The validation process involves comparing the nondimensional half-length and maximum diameter of the supercavity for various cavitation numbers. The variation of nondimensional supercavity length with cavitation number is shown in Figure 5(a), and the nondimensional maximum diameter at various cavitation numbers is shown in Figure 5(b). The dotted line in Figure 5 represents the quadratic polynomial curve fit for the computational data. The computational data exhibit a strong agreement with the experimental data, yielding RMSE values of 4.62% and 4.01% for the nondimensional half-length and maximum diameter of the supercavity, respectively.

3 Results and discussions

The following section presents the results of the numerical simulations conducted to evaluate the impact of the secondary cavitator on supercavitation characteristics. The performance of various cavitator configurations is also assessed in terms of supercavity geometry under different operational conditions. The analysis focuses on the effects of primary and secondary cavitators' size, positioning, and Froude number on the overall supercavity dynamics.

3.1 Supercavity formation with primary cavitator

This section discusses the characteristics of the supercavity generated by the primary cavitator. The supercavity formation is initiated by the cavitator mounted at the nose of the torpedo, as shown in Figure 6. The growth and stability of the supercavity are governed by the balance between the pressure gradient in the flow and the inertia of the surrounding fluid. As the flow upstream of the primary cavitator is deflected outward, the resulting expansion energy forms the supercavity (Semenenko, 2001).

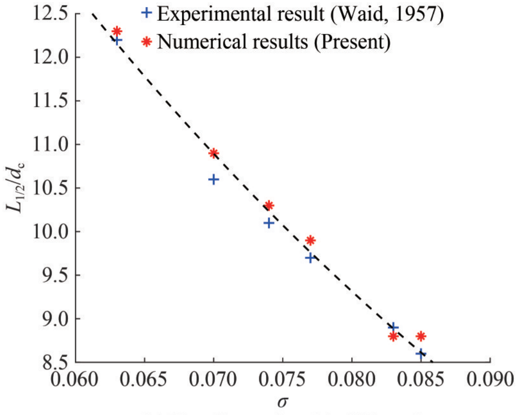

(a) Nondimensional half-length

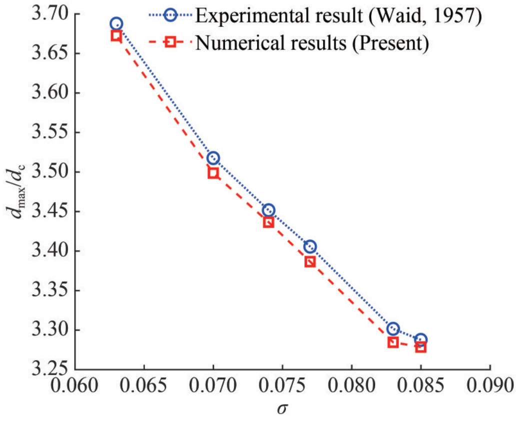

(b) Nondimensional maximum diameter

Figure 5 Comparison of the supercavity's geometrical characteristics at various cavitation numbers obtained from the computational results of the present study validated against the experimental result reported by Waid (1957)

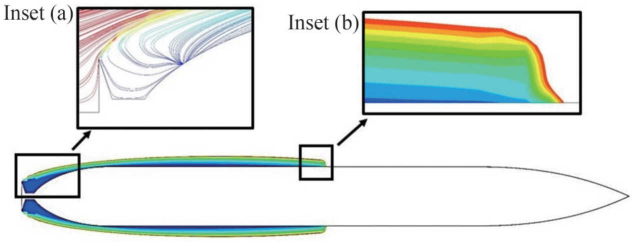

Figure 6 Flow properties of the supercavity generated by the primary cavitator. Inset (a) shows streamlines near the primary cavitator. Inset (b) shows a closeup of the supercavity closure

Inset (a) of Figure 6 illustrates the streamlines near the primary cavitator, revealing a water vapor circulation zone that forms behind the cavitator due to the upstream movement of vapor caused by the adverse pressure gradient. Inset (b) shows a closeup view of the supercavity geometry at its closure. At this point, the vapor has dissipated much of its energy and can no longer overcome the pressure force exerted by the surrounding liquid, causing it to travel upstream and form a recirculation zone. The vapor gradually condenses back to liquid at the closure point, resulting in an axisymmetric cavity shape. Referred to as reentrant jets (Semenenko, 2001), such closures are common in supercavitation.

The primary cavitator's diameter significantly affects the supercavity geometry. Large cavitators tend to produce extra elongated cavities but introduce high drag. Therefore, a tradeoff exists between cavity size and drag, necessitating further optimization for efficient operation. Although the primary cavitator alone can generate a supercavity, its limitations become evident at low speeds or under certain operational conditions. Hence, additional techniques, such as the introduction of a secondary cavitator, are warranted.

3.2 Influence of secondary cavitator on supercavity enhancement

A secondary cavitator is introduced downstream to overcome the limitations of the primary cavitator and further increase the supercavity size. This secondary cavitator alters the flow dynamics and interacts with the primary supercavity, significantly influencing the geometry of the overall cavity. When optimally positioned, the secondary cavitator generates a secondary supercavity that merges with the primary cavity, forming a large and stable coalesced supercavity.

Analysis of the flow near the secondary cavitator shows that it diverts water vapor toward the periphery of the supercavity, as depicted in Figure 7. This diversion expands the boundaries of the supercavity, effectively increasing its size. The influence of the secondary cavitator in expanding the supercavity is particularly useful at low speeds, where the primary cavitator alone may not generate a sufficiently large cavity.

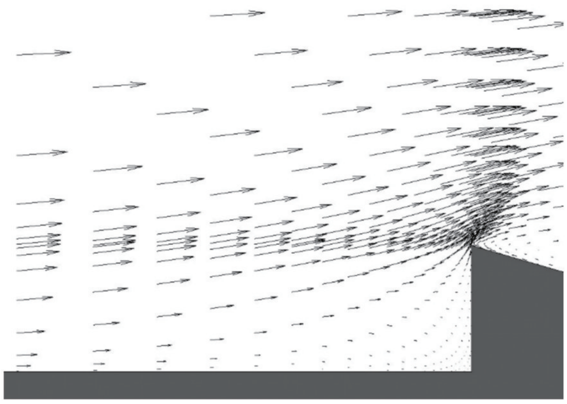

Figure 7 Velocity vectors near the secondary cavitator, illustrating the flow deflecting toward the periphery of the supercavity and thus contributing to the expansion of the cavity's boundary

However, careful optimization of the secondary cavitator's size and positioning is necessary to avoid negative effects. If the secondary cavitator exceeds a critical size, the water stream will strike the cavitator, resulting in a reverse flow that forms a powerful jet. This reverse flow leads to the shrinkage of the primary supercavity, producing a separate, unmerged secondary cavity. In such cases, the failure to coalesce the cavities results in increased, rather than reduced, drag. Optimizing the placement and size of the secondary cavitator can maximize the amplification of the supercavity, particularly at low operational speeds where the primary cavitator's effect is limited.

A detailed analysis of the optimization of these parameters and their effects on supercavity amplification is presented in Sections 3.3–3.5.

3.3 Optimal positioning of secondary cavitator for maximum supercavity amplification

Simulations are conducted by positioning the cavitator at 35%, 45%, 55%, and 65% of the torpedo length to optimize the placement of the secondary cavitator along the torpedo's length. The primary cavitator's diameter $\tilde{d}_{\mathrm{cv}}$ is 0.4, and the secondary cavitator's height $\tilde{d}_{\mathrm{sp}}$ is 0.04. The Froude number (*Fr*) for these simulations is varied between 5 and 6.

An "amplification factor" (η) is introduced to quantify the enlargement in supercavity size due to the addition of the secondary cavitator. The amplification factor is defined as the ratio of the total length of the coalesced supercavity $\left(L_c\right)$ to the original length of the supercavity formed by the primary cavitator alone $\left(L_{\mathrm{cp}}\right)$ as mentioned in Eq. (12).

$$\eta = \frac{L_c}{L_{\mathrm{cp}}} \tag{12}$$

The highest amplification is achieved at different secondary cavitator locations depending on the flow conditions. For example, at a Froude number of 5, the maximum amplification occurs when the secondary cavitator is placed at 35% of the primary supercavity length. Conversely, at a Froude number of 6, the highest amplification is observed when the secondary cavitator is placed at 65% of the primary supercavity length. These results indicate that the optimal location of the secondary cavitator is dependent on the Froude number and hence on the size of the primary supercavity.

To further explore this relationship, the amplification factor is plotted as a function of the secondary cavitator location, expressed as a percentage of the primary supercavity length X_{cs} for all the cases. Four distinct zones can be seen in Figure 8.

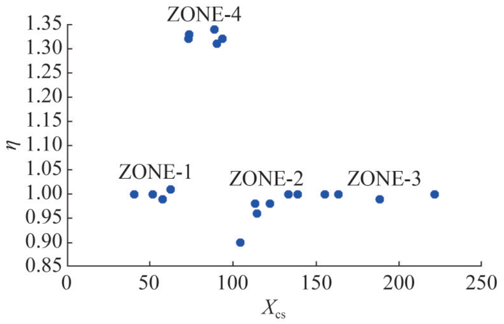

Figure 8 Variation of amplification factor (η) with the location of secondary cavitator, expressed as a percentage of primary supercavity length (X_{cs})

- Zone 1: Secondary Cavitator Within the Primary Supercavity

When the secondary cavitator is placed inside the primary supercavity, i.e., between 40% and 80% of the primary supercavity length, it remains in contact with the vapor phase and does not interact with seawater. In this configuration, a secondary supercavity does not form as shown in Figure 9(a).

- Zone 2: Secondary Cavitator Placed Immediately After the Primary Supercavity

When the secondary cavitator is positioned just beyond the primary supercavity, i.e., between 100% and 125% of the primary supercavity length, the incoming water stream strikes the secondary cavitator, producing a strong reverse jet that suppresses the primary supercavity. This water jet disturbs the closure of the primary cavity and thus suppresses it, as depicted in Figure 9(b).

- Zone 3: Secondary Cavitator Positioned Far from the Primary Supercavity

When the secondary cavitator is placed at a great distance from the primary supercavity, i.e., between 125% and 225% of its length, a secondary supercavity forms. However, Figure 9(c) shows that in this configuration, the primary and secondary supercavities remain separate without any interaction between them.

- Zone 4: Secondary Cavitator at the Closure of the Primary Supercavity

When the secondary cavitator is located near the closure of the primary supercavity, i.e., between 70% and 90% of the primary supercavity length, a secondary supercavity is generated. In this scenario, the primary and secondary supercavities coalesce, forming a significantly large, unified supercavity as illustrated by Figure 9(d).

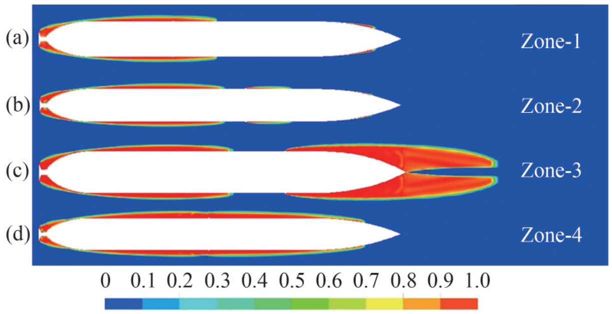

Figure 9 Volume fraction contour of vapor phase for different zones

On the basis of these observations, the secondary cavitator should be positioned between 70% and 90% of the primary supercavity length to achieve an amplified and enlarged supercavity. This placement ensures the coalescence of the primary and secondary supercavities, resulting in the formation of a large, continuous cavity.

3.4 Critical size of secondary cavitator for enhanced supercavitation

For the optimization of the secondary cavitator's size, its height $\tilde{d}_{\mathrm{sp}}$ is varied from 0.01 to 0.08. The simulations are conducted at $\tilde{d}_{\mathrm{cv}}$ of 0.45 and Fr of 5.5. During these simulations, the secondary cavitator is placed at 80% of the primary supercavity length. The contour of the volume fraction of vapor is shown in Figure 10. The amplification factor (η) increases with $\tilde{d}_{\mathrm{sp}}$ up to a certain limit (Figures 10(a), 10(b), 10(c) and 10(d)). When the amplification factor reaches its maximum value (Figure 10(e)), the corresponding $\tilde{d}_{\mathrm{sp}}$ is termed as critical $\tilde{d}_{\mathrm{sp}}$ ($\tilde{d}^*_{\mathrm{sp}}$). The supercavity length increases because the secondary cavitator deflects the vapor away from the surface, causing the expansion of the vapor, which in turn increases the supercavity size. Further increasing the value of $\tilde{d}_{\mathrm{sp}}$ initiates the formation of water jets in the upstream direction, which quickly and prominently suppresses the primary supercavity as shown in Figure 10(f). Although the large size of the secondary cavitator allows it to form a large secondary supercavity, the secondary cavity does not merge with the primary supercavity. In such cases, even with the presence of a large secondary cavity, the surface of the torpedo upstream of the secondary cavitator remains in contact with water as shown in Figures 10(g), 10(h) and 10(i).

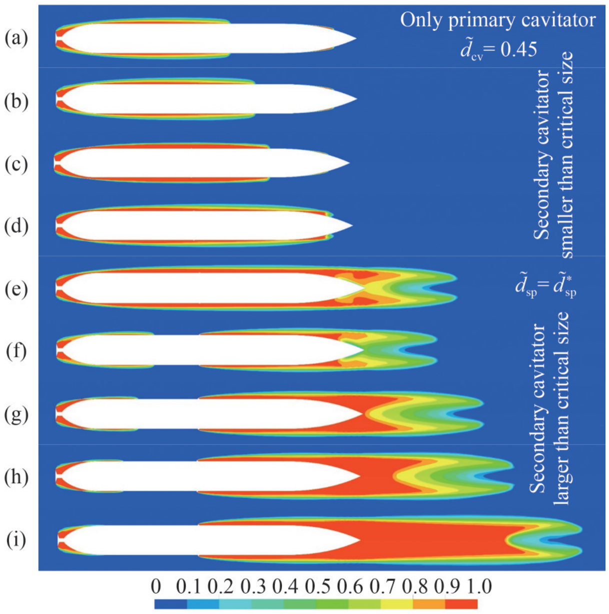

Figure 10 Contour of the volume fraction of water vapor over the torpedo with the primary cavitator's $\tilde{d}_{\mathrm{cv}}$ = 0.45 at Fr = 5.5 and secondary cavitator's diameter $\tilde{d}_{\mathrm{sp}}$ of (a) no secondary cavitator, (b) 0.01, (c) 0.02, (d) 0.03, (e) 0.04, (f) 0.05, (g) 0.06, (h) 0.07 and (i) 0.08

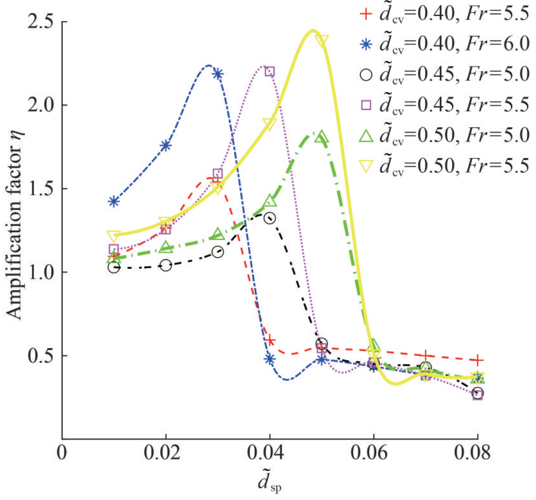

Figure 11 Variation of amplification factor (η) with $\tilde{d}_{\mathrm{sp}}$

3.5 Influence of primary cavitator and froude number on supercavity behavior

To investigate the dependence of the optimal secondary cavitator size ($\tilde{d}^*_{\mathrm{sp}}$) on the primary cavitator size and Froude number (Fr), simulations are performed for various combinations of $\tilde{d}_{\mathrm{cv}}$ and Fr. The amplification factor is plotted against $\tilde{d}_{\mathrm{sp}}$ for all the cases, as shown in Figure 11. A consistent trend is observed across all cases, where the amplification factor initially increases with $\tilde{d}_{\mathrm{sp}}$ before reaching a peak and then decreasing.

However, the peak of the amplification factor curves shifts as $\tilde{d}_{\mathrm{cv}}$ varies, indicating that the secondary cavitator's optimal size is dependent on the primary cavitator's size. $\tilde{d}^*_{\mathrm{sp}}$ is plotted against $\tilde{d}_{\mathrm{cv}}$ as shown in Figure 12 to further explore this relationship. A clear trend is observed: as the size of the primary cavitator ($\tilde{d}_{\mathrm{cv}}$) increased, the value of $\tilde{d}^*_{\mathrm{sp}}$ also increased.

3.6 Dependence of amplification factor (η) on froude number (Fr)

A series of numerical simulations is conducted to gain a deep understanding of the influence of the Froude number on the amplification factor. In these simulations, the primary cavitator's diameter is fixed at $\tilde{d}_{\mathrm{cv}}$ = 0.5. The secondary cavitator's diameter is set to the critical height, $\tilde{d}^*_{\mathrm{sp}}$ = 0.05, as determined for this configuration. The simulations span a Froude number range of 4.75 – 6.0 and are carried out with and without the presence of the secondary cavitator. The resulting supercavity lengths in both configurations are compared, and the amplification factor is computed accordingly. Figure 13 presents the variation of the amplification factor as a function of the Froude number. The

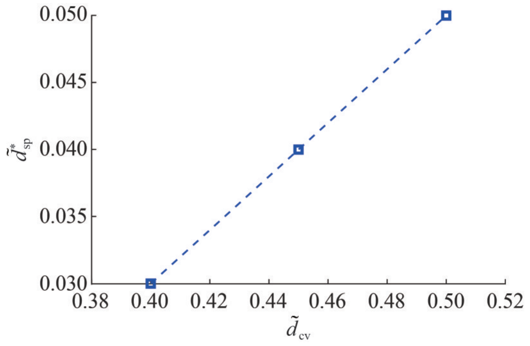

Figure 12 Variation of critical $\tilde{d}_{sp}$ $\left(\tilde{d}^*_{sp}\right)$ with the primary cavitator diameter $\left(\tilde{d}_{cv}\right)$. Note that each data point is obtained from eight distinct simulations

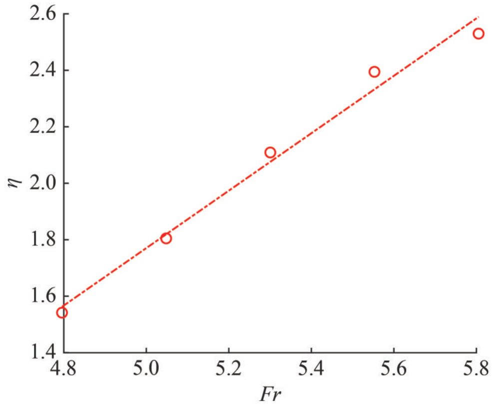

Figure 13 Variation of amplification factor (η) with the Froude number (Fr)

plot indicates a linear increase in the amplification factor with the rising Froude number, suggesting a proportional relationship between these two parameters.

4 Conclusions

This study introduces a novel approach of installing a secondary cavitator on the torpedo's surface to enhance the performance of supercavitating torpedoes. Simulations are conducted across various geometries, exploring different primary cavitator diameters, secondary cavitator locations and sizes, and Froude numbers. The secondary cavitator interacts with the primary supercavity, significantly influencing the latter's geometric characteristics. Positioning the secondary cavitator at 70%–90% of the primary supercavity length can prominently amplify the supercavity size, achieving an increase of 30%–35% in cavity length.

The size of the secondary cavitator plays a critical role in supercavity formation. When the secondary cavitator size is below the critical threshold, the secondary supercavity merges with the primary one, creating a large, coalesced supercavity. Increasing the height of the secondary cavitator further enlarges this coalesced cavity. However, when its size exceeds the critical value, the secondary cavitator suppresses the primary supercavity. An unmerged, separate secondary cavity consequently forms. This study also extensively investigates the dependence of the secondary cavitator's critical size on the primary cavitator's diameter and Froude number, providing valuable insights into the factors influencing supercavity stability and drag reduction.

The findings contribute to the development of efficient supercavitating torpedoes. The integration of secondary cavitators provides new design possibilities for supercavitating vehicles and offers a practical framework for optimizing cavitator configurations. This research demonstrates the potential to convert existing heavyweight torpedoes into supercavitating torpedoes. Future work may focus on optimizing the cavitator shape, exploring the underlying physics and fundamental phenomena involved, and quantifying the effects of flow unsteadiness on the performance of the secondary cavitator. The impact of the secondary cavitator on the propulsion system of the torpedo and its stability and control should be explored. A 3D computational study may reveal interesting phenomena. The influence of the torpedo's angle of attack on the behavior and effectiveness of the secondary cavitator should also be investigated in subsequent studies.

Acknowledgement We express our heartfelt gratitude to the UPES, Dehradun, for providing the necessary resources and support to carry out this research.

Competing interest The authors have no competing interests to declare that are relevant to the content of this article.

References

Alyanak E, Grandhi R, Penmetsa R (2006) Optimum design of a supercavitating torpedo considering overall size, shape, and structural configuration. International Journal of Solids and Structures 43(3): 642-657. https://doi.org/10.1016/j.ijsolstr.2005.05.040

Cao L, Karn A, Arndt RE, Wang Z, Hong J (2017) Numerical investigations of pressure distribution inside a ventilated supercavity. Journal of Fluids Engineering 139(2): 021301

Chen G, Sun T, Yang ZHT (2023) A study on the cavitating flow around an elliptical disk-shaped cavitator for non-body-of-revolution underwater vehicles. Engineering Applications of Computational Fluid Mechanics 17(1): 2159882. https://doi.org/10.1080/19942060.2022.2159882

Dular M, Griessler-Bulc T, Gutierrez-Aguirre I, Heath E, Kosjek T, Krivograd Klemenčič A, Oder M, Petkovšek M, Rački N, Ravnikar M, Šarc A, Širok B, Zupanc M, Žitnik M, Kompare B (2016) Use of hydrodynamic cavitation in (waste) water treatment. Ultrasonics Sonochemistry 29: 577-588. https://doi.org/10.1016/j.ultsonch.2015.10.010

Gaurav K, Mittal G, Karn A (2022) On the morphology of elongated bubbles during their formation at submerged orifices. Chemical Engineering Science 250: 117395. https://doi.org/10.1016/j.ces.2021.117395

Gaurav K, Venkatesh N, Karn A (2024) A comparative assessment of various cavitator shapes for high-speed supercavitating torpedoes: Geometry, flow-physics and drag considerations. Journal of Applied Fluid Mechanics 17(9): 2028-2044. https://doi.org/10.47176/jafm.17.9.2631

Jeong SW, Pham VD, Ahn BK, Paik BG (2024) Experimental and numerical study on flow dynamics and universal characteristics of ventilated supercavities behind different cavitators. International Journal of Naval Architecture and Ocean Engineering 16: 100582. https://doi.org/10.1016/j.ijnaoe.2024.100582

Karn A, Chawdhary S (2018) On the synergistic interrelation between supercavity formation through vaporous and ventilated routes. International Journal of Multiphase Flow 104: 1-8. https://doi.org/10.1016/j.ijmultiphaseflow.2018.03.015

Karn A, Rosiejka B (2017) Air entrainment characteristics of artificial supercavities for free and constrained closure models. Experimental Thermal and Fluid Science 81: 364-369. https://doi.org/10.1016/j.expthermflusci.2016.10.003

Kim MJ, Kim SH, Lee KC, Paik BG, Kim MC (2021) Cavitator design for straight-running supercavitating torpedoes. Applied Sciences 11(14): 6247. https://doi.org/10.3390/app11146247

Kim S, Lee J, Lee H, Lim J, Cho J (2022) Effect of rotating, non-axisymmetric cavitator on supercavity size. Journal of Mechanical Science and Technology 36(7): 3437-3447. Scopus. https://doi.org/10.1007/s12206-022-0622-8

Li D, Chen W, Shi Y, Luo K (2022) Bow rudder of cavitator attached with a non-symmetric anti-roll fin for strong manoeuvring underwater supercavitating vehicles. Ships and Offshore Structures 17(4): 840-851. https://doi.org/10.1080/17445302.2021.1878755

Likhachev DS, Li F, Kulagin VA (2014) Experimental study on the performance of a rotational supercavitating evaporator for desalination. Science China Technological Sciences 57(11): 2115-2130. https://doi.org/10.1007/s11431-014-5631-0

Liu B, Xiang M, Xie Z, Zhang W (2023) On ventilated supercavities moving horizontally near free surface. Ocean Engineering 267: 113229. https://doi.org/10.1016/j.oceaneng.2022.113229

Logvinovich G, Serebryakov V (1975) On methods of calculating form of slender axisymmetric cavities. J. Hydromechanics 32: 47-54

Myring DF (1976) Theoretical study of body drag in subcritical axisymmetric flow. Aeronautical Quarterly 27(3): 186-194. https://doi.org/10.1017/S000192590000768X

Nesteruk I (2012) Supercavitation: Advances and Perspectives A collection dedicated to the 70th jubilee of Yu. N. Savchenko. Springer, Berlin

Nguyen VT, Park WG (2022) Numerical study of the thermodynamics and supercavitating flow around an underwater high-speed projectile using a fully compressible multiphase flow model. Ocean Engineering 257: 111686. https://doi.org/10.1016/j.oceaneng.2022.111686

Park SH, Nguyen VT, Park WG (2024) Numerical investigation on supercavitation hydrodynamics of high-speed water entry projectiles under effect of different head shapes. Ocean Engineering 311: 118926. https://doi.org/10.1016/j.oceaneng.2024.118926

Rajkumar R, Gaurav K, Karn A, Kumar V, Shukla H (2023) Numerical investigation of the effect of liquid temperature on supercavitation. In Narendranth S, Mukunda PG, Saha UK (Eds.), Recent Advances in Mechanical Engineering, Springer, Berlin, 19-27. https://doi.org/10.1007/978-981-19-1388-4_2

Schmid A (2010) New jet-aeration system using ‘Supercavitation’. Environmental Science and Pollution Research 17(3): 582-585. https://doi.org/10.1007/s11356-009-0199-0

Schnerr GH, Sauer J (2001) Physical and numerical modeling of unsteady cavitation dynamics. Proceedings of 4th International Conference on Multiphase Flow, New Orleans, USA

Semenenko VN (2001) Artificial supercavitation. Physics and Calculation. Available from https://apps. dtic. mil/sti/citations/tr/ADP012080 [Accessed on Mar. 14, 2024]

Shao S, Balakrishna A, Yoon K, Li J, Liu Y, Hong J (2020) Effect of mounting strut and cavitator shape on the ventilation demand for ventilated supercavitation. Experimental Thermal and Fluid Science 118: 110173. https://doi.org/10.1016/j. expthermflusci.2020.110173

Sun X, You W, Xuan X, Ji L, Xu X, Wang G, Zhao S, Boczkaj G, Yoon JY, Chen S (2021) Effect of the cavitation generation unit structure on the performance of an advanced hydrodynamic cavitation reactor for process intensifications. Chemical Engineering Journal 412: 128600. https://doi.org/10.1016/j.cej.2021.128600

Waid RL (1957) Cavity shapes for circular disks at angles of attack. Available from https://authors. library. caltech. edu/records/cape9-a2b62 [Accessed on Feb. 11, 2024]

Xu C, Khoo BC (2020) Dynamics of the supercavitating hydrofoil with cavitator in steady flow field. Physics of Fluids 32(12): 123307. https://doi.org/10.1063/5.0030907

Yi JJ, Kim MJ, Kim SH, Paik BG, Kim KC (2022) Prediction of supercavitation shapes for a wide range of Froude numbers. International Journal of Naval Architecture and Ocean Engineering 14: 100426. https://doi.org/10.1016/j.ijnaoe.2021. 11.009